www.sciencemag.org/content/361/6408/1252/suppl/DC1

Supplementary Materials for

Programmable protein circuits in living cells

Xiaojing J. Gao*, Lucy S. Chong*, Matthew S. Kim, Michael B. Elowitz†

*These authors contributed equally to this work.
†Corresponding author. Email: melowitz@caltech.edu

Published 21 September 2018, *Science* **361**, 1252 (2018)
DOI: 10.1126/science.aat5062

This PDF file includes:

Other Supplementary Material for this manuscript includes the following:
(available at www.sciencemag.org/content/361/6408/1252/suppl/DC1)

Table S1 (.xlsx)
Movie S1 (.mov)

Materials and Methods

Plasmid construction

All constructs were generated using standard procedures. The backbones were linearized using restriction digestion or PCR, and inserts were generated using PCR or gBlock synthesis (IDT). A list of all plasmids reported in this manuscript is included in Table S1, and all plasmids and maps are deposited with Addgene.

Tissue culture

The Flp-In™ T-REx™ 293 Cell Line (Human Embryonic Kidney cells that contain a single stably integrated FRT site at a transcriptionally active genomic locus, and stably expressing the tetracycline repressor protein) was purchased from Thermo Fisher Scientific (R78007). Cells were cultured in a humidity controlled chamber at 37°C with 5% CO_2 in media containing DMEM supplemented with 10% FBS, 1 mM sodium pyruvate, 1 unit/ml penicillin, 1 µg/ml streptomycin, 2 mM L-glutamine and 1X MEM non-essential amino acids. 100 ng/mL doxycycline was added whenever expression is needed from a CMV-TO promoter. All stably integrated transgenes were inducible with doxycycline, which was only added one day before characterization. Trimethoprim (TMP) was delivered at 1 µM. Rapamycin was delivered at 5 nM. Epidermal growth factor (EGF) was delivered at 25 ng/mL. SHIELD1 was delivered at 1 µM. ASV was delivered at 3 µM. For bulk measurement of pulsing dynamics, cells were cultured in the presence of 40 µM biliverdin, and rapamycin was added at different time points before preparation for flow cytometry. For stimulation with EGF, cells were cultured to near 100% confluency before transfection, and, one day after transfection, exposed to 40 µM biliverdin, 25 ng/mL EGF, and 100 ng/mL doxycycline for 6 hours prior to flow cytometry analysis.

Transient transfection

293 cells were seeded at a density of 0.05×10^6 cells per well of a 24-well plate and cultured under standard conditions overnight. The following day, the cells were transfected with plasmid constructs using Lipofectamine 2000 (Thermo Fisher) as per manufacturer's protocol.

Flow cytometry

Two days after transfection, cells were prepared for flow cytometry by trypsinizing with 30µL of 0.05% trypsin for 1 min at room temperature. Protease activity was neutralized by resuspending the cells in buffer containing 70 µL of HBSS with 2.5mg/ml Bovine Serum Albumin (BSA). For cells stimulated with EGF, cells were resuspended in buffer containing 70µL of HBSS with 2.5 mg/mL BSA and 1 mM EDTA. Cells were then filtered through a 40 µm cell strainer and analyzed by flow cytometry (MACSQuant VYB, Miltenyi or CytoFLEX, Beckman Coulter). We used the EasyFlow Matlab-based software package developed in-house by Yaron Antebi to process flow cytometry data.

Annexin V staining

Staining was performed using a standard kit (ThermoFisher A13201). One day after transfection, cell culture medium was removed from each well, and replaced with 7.5 µL FITC-conjugated annexin V within 150 µL binding buffer. After incubation in dark at 37°C for 15 min, the staining medium was removed, and the cells trypsinized for flow cytometry analysis.

Fluorescent signal quantification from flow cytometric measurements

To maximize the observable reporter dynamic range, we selected and compared cells with the highest expression of the co-transfection marker, which showed the largest separation of basal reporter fluorescence from cellular autofluorescence. For each sample in a comparison group (experiments performed in the same batch and data shown on the same plot), we calculated the 98 and 99.5 percentiles of fluorescence of the co-transfection marker (mCherry in most cases). We identified the sample with the lowest 98 percentile value, and used its 98 and 99.5 percentiles as lower and upper limits to gate on all samples. For all cells within the gate in each sample, we fit the distribution of the logarithm of their signal fluorescence (Citrine in most cases) with skew Gaussian distributions, i.e. N*normcdf(x,m,k)*normpdf(x,m,s) in Matlab using non-linear least-square fitting, and reported the mode (peak position, representing the reporter level that's most likely to be observed) of the resulting fit (Fig. S1A). Here, the normcdf(x,µ,σ) and normpdf(x,µ,σ) functions are cumulative probability density and probability density functions for a Gaussian distribution respectively, and the parameter n is a normalization factor, m=µ is the mean of the Gaussian function, s=σ is the inverse standard deviation of the Gaussian, and k parameterizes skewness. No gating was performed on monoclonal cells with the genomically integrated pulsing circuit, because, unlike transient transfection, here expression variation is already limited.

Calculating reduction index from flow cytometric measurements

To calculate the reduction of cell numbers, we compared the effects of various treatments on cell numbers, comparing each measurement to a negative control transfected with only a fluorescent marker, and using the size of the untransfected cell population for internal normalization. To do this, we proceeded in several steps: First, we fit the distribution of the logarithm of autofluorescence collected in the Citrine channel from mock transfected cells with the MATLAB function N_0*normcdf(x,m_0,k_0) *normpdf(x,m_0,s_0) using non-linear least-square fitting. Here, the parameters n_0, m_0, s_0, and k_0 and functions normcdf() and normpdf() have the same meanings as in the previous section. Reference values for m_0, s_0, k_0, were thus determined from measurement of autofluorescence in untransfected cells and fixed for subsequent two-component model fits. Second, for each transfected well, we fit the distribution of the logarithm of Citrine signal with N_1*normcdf(x,m_0,k_0)* normpdf (x,m_0,s_0) +N_2*normpdf(x,m_2,s_2), where N_1, N_2, m_2, s_2 were free parameters and m_0, s_0, k_0 were fixed to values extracted from autofluorescence fit. The area under the curve N_1* normcdf(x,m_0,k_0)*normpdf(x,m_0,s_0) ("area a_0" and "area a" in Fig. S5B) corresponds to the number of untransfected cells, which serves as an internal reference. Third, we subtracted the number of untransfected cells from the total number of cells to get the number of transfected cells that survived ("area b_0" and "area b" in Fig. S5B). For each sample, the number of transfected cells that survived was then normalized to the number of untransfected

cells, and the ratio between normalized survival number in that condition ((area a)/(area b) in Fig. S5B) and normalized survival number in the Citrine-only control condition ((area a_0)/(area b_0) in Fig. S5B) was defined as survival percentage. Finally, the reduction index was defined as 1-survival percentage.

In experiments with SOS_{CA} cells, a small fraction of these cells silenced their transgene expression during cell culture. To make sure that we were only analyzing cells that do express a Ras activator, we gated on mCherry that's co-expressed with SOS_{CA}, and excluded the mCherry– population. This co-expressed mCherry marker was also utilized in co-culture experiments, to distinguish SOS_{CA}/EGFRvIII cells from control cells, so that we could calculate their reduction index separately.

Mathematical modeling of the bandpass circuit

To analyze the behavior of the bandpass circuit, we constructed a minimal ordinary differential equation model representing the key components and interactions within the circuit. The model incorporated three types of interactions: protein production, first-order degradation, and cleavage by proteases. In the model, protease regulation of substrates is described by differential equations of the following form:

$$\frac{d[Substrate]}{dt} = A - k_{cat}^{Protease}[Protease][Substrate] - k_{dA}[Substrate] \quad (1)$$

$$\frac{d[Substrate_{cleaved}]}{dt} = k_{cat}^{Protease}[Protease][Substrate] - k_{dB}[Substrate_{cleaved}] \quad (2)$$

Here, A represents the production rate of a proteolytic substrate, $k_{cat}^{Protease}$ represents the catalytic coefficient, assuming that proteolysis can be described as a Michaelis-Menten reaction far from saturation, and the first-order degradation rates k_{dA} and k_{dB} represent degradation through basal cellular degradation pathways. These rate constants can take higher or lower values depending on whether the substrate protein and its cleaved form are unstable or stable, respectively.

To simplify the analysis without loss of generality, we set $A = 1$ in the equations for fluorescent reporters, effectively using arbitrary normalized units for the fluorescent protein concentrations. [Substrate] in the normalized version thus corresponds to [Substrate]/A in the original version.

We first considered a Cit_{DHFR} reporter, whose DHFR degron can be removed by TEVP with a coefficient k_{cat}^{TE}. In its initial form, the reporter degrades at rate k_{d1} (Equation 3), while its cleaved product, Cit, degrades at a rate k_{d2} (Equation 4).

$$\frac{dCit_{DHFR}}{dt} = 1 - k_{cat}^{TE}[TEVP][Cit_{DHFR}] - k_{d1}[Cit_{DHFR}] \quad (3)$$

$$\frac{dCit}{dt} = k_{cat}^{TE}[TEVP][Cit_{DHFR}] - k_{d2}[Cit] \quad (4)$$

The steady-state solutions for Eqs. 3, 4 are:

$$Cit_{DHFR} = \frac{1}{k_{cat}^{TE}[TEVP] + k_{d1}} \quad (5)$$

$$Cit = \frac{k_{cat}^{TE}[TEVP]}{k_{d2}(k_{cat}^{TE}[TEVP] + k_{d1})} \quad (6)$$

Experimentally measured reporter fluorescence corresponds to the sum $Cit_{DHFR} + Cit$. The absolute value of the independent variable [TEVP] is not known. However, based on experiments in which protein expression levels correlated linearly with the amount of transfected plasmid (Fig. S4A), we substituted the concentration of transfected plasmid, p_{TE}, for $[TEVP]$ in all equations, effectively absorbing the constant of proportionality relating [TEVP] and p_{TE} into the k_{cat}^{TE} values. With these simplifications, measured fluorescence can be written:

$$Cit_{total} = Cit_{DHFR} + Cit = \frac{\frac{k_{cat}^{TE}p_{TE}}{k_{d2}} + 1}{k_{cat}^{TE}p_{TE} + k_{d1}} \quad (7)$$

Using Matlab's curve fitting toolbox, we determined best fit values of the parameters k_{cat}^{TE}, k_{d1} and k_{d2} by fitting Eq. 7 to the experimentally measured p_{TE}- Cit_{total} curve (Fig. 3B).

To model the repression arm of the bandpass circuit, we must take into account the mutual inhibitory activities of TVMVP and HCVP in the circuit. These protease-protease equations take on the general form outlined in Eqs 1, 2. However, because reporter and protease concentrations are measured in different units (fluorescence and plasmid concentration, respectively), their production rates cannot both be arbitrarily set to 1. Instead, we denoted the protease production rate B, to account for the different units used for these two species. Specifically, for 1 unit of plasmid input to produce 1 unit of protease at steady-state, B must equal the degradation rate of the protease multiplied by the amount of plasmid input ($p_{Protease}$), as shown below in Equations 8 and 9.

$$\frac{d[TVMVP]}{dt} = k_{dTV}p_{TV} - k_{cat}^{HC}[HCVP][TVMVP] - k_{dTV}[TVMVP] \quad (8)$$

$$\frac{d[HCVP]}{dt} = k_{dHC}p_{HC} - k_{cat}^{TV}[TVMVP][HCVP] - k_{dHC}[HCVP] \quad (9)$$

At steady-state, the concentration of TVMV protease can be expressed as a function of the plasmid inputs of TVMVP and HCVP:

$$[TVMVP] = \frac{W + (W^2 + 4k_{cat}^{TV}k_{dTV}^2 k_{dHC}p_{TV})^{\frac{1}{2}}}{2k_{cat}^{TV}k_{dTV}} \quad (10)$$

where $W \equiv k_{dTV}k_{cat}^{TV}p_{TV} - k_{dHC}k_{dTV} - k_{cat}^{HC}k_{dHC}p_{HC}$. The reporter repressed by TVMVP is denoted Cit when not cleaved (first-order degradation rate k_{d3}), and Cit_{Ndeg} when cleaved by TVMVP to expose an N-end degron (first-order degradation rate k_{d4}).We then used a procedure similar to Eqs. 3-7 to express reporter expressions in terms of [TVMVP]:

$$Cit = \frac{1}{k_{cat}^{TV}[TVMVP] + k_{d3}} \quad (11^*)$$

$$Cit_{Ndeg} = \frac{k_{cat}^{TV}[TVMVP]}{k_{d4}(k_{cat}^{TV}[TVMVP] + k_{d3})} \quad (12^*)$$

$$Cit_{total} = \frac{\frac{k_{cat}^{TV}[TVMVP]}{k_{d4}} + 1}{k_{cat}^{TV}[TVMVP] + k_{d3}} \quad (13^*)$$

* For all equations denoted with "*", [TVMVP] takes the value defined in Eq. 10.

We estimated the values of parameters, $k_{cat}^{HC}, k_{cat}^{TV}, k_{dHC}, k_{dTV}, k_{d3}, k_{d4}$, by fitting Eq. 13 to experimentally measured Cit_{total}, p_{TV}, and p_{HC} (Fig. 3C).

To characterize the cooperativity caused by TVMVP-HCVP mutual inhibition, we fit the repression curves in Fig. 3C with a sigmoidal function:

$$Cit_{total} = \frac{C}{1 + \left(\frac{p_{TV}}{K}\right)^n} \quad (14)$$

The 95% confidence intervals for the Hill coefficient, n, were $0.95 \pm 0.13, 2.0 \pm 0.4, and\ 2.4 \pm 0.5$, for p_{HC} values of 0, 50, and 200 ng, respectively.

Finally, for the reporter that's simultaneously regulated by the activation and repression arms, depending on whether the DHFR degron is removed and whether the N-end degron is exposed, there are four possible species Cit_{DHFR}, $Cit_{DHFR+Ndeg}$, Cit, and Cit_{Ndeg}, the first-order degradation rates of which we denote as k_{dA}, k_{dB}, k_{dC}, and k_{dD}, respectively. Similarly, the dynamics of these four species can be expressed as:

$$\frac{dCit_{DHFR}}{dt} = 1 - k_{cat}^{TE}[TEVP][Cit_{DHFR}] - k_{cat}^{TV}[TVMVP][Cit_{DHFR}] - k_{dA}[Cit_{DHFR}] \quad (15^*)$$

$$\frac{dCit_{DHFR+Ndeg}}{dt} = k_{cat}^{TV}[TVMVP][Cit_{DHFR}] - k_{cat}^{TE}[TEVP]\left[Cit_{DHFR+Ndeg}\right] - k_{dB}\left[Cit_{DHFR+Ndeg}\right] \quad (16^*)$$

$$\frac{dCit}{dt} = k_{cat}^{TE}[TEVP][Cit_{DHFR}] - k_{cat}^{TV}[TVMVP][Cit] - k_{dC}[Cit] \quad (17^*)$$

$$\frac{dCit_{Ndeg}}{dt} = k_{cat}^{TE}[TEVP]\left[Cit_{DHFR+Ndeg}\right] + k_{cat}^{TV}[TVMVP][Cit] - k_{dD}\left[Cit_{Ndeg}\right] \qquad (18^*)$$

We summed the steady-state solutions of all species from these equations to derive the final input-output equation for the bandpass circuit:

$$Cit_{total} = \frac{1 + X + Y + \frac{k_{cat}^{TE}p_{TE}X + k_{cat}^{TV}[TVMVP]Y}{k_{dD}}}{k_{cat}^{TE}p_{TE} + k_{cat}^{TV}[TVMVP] + k_{dA}}, \qquad (19^*)$$

Where $X \equiv \frac{k_{cat}^{TV}[TVMVP]}{k_{cat}^{TE}p_{TE}+k_{dB}}$ and $Y \equiv \frac{k_{cat}^{TE}p_{TE}}{k_{cat}^{TV}[TVMVP]+k_{dC}}$

We used this equation to fit the experimentally observed bandpass behavior (Figure 3D).

Cell line construction

Some of the experiments do require more stable/homogenous transgene expression, for which we used antibiotic selection to generate cell lines with stably integrated transgenes. Two days after transfection in 24-well plates, cells were transferred to 6-well plate and selected with either 50 µg/mL Hygromycin (Hyg) or 400 µg/mL Geneticin (Gen). SOS_{CA} cells: CMV-TO-MSos-2A-H2BChe-FlpIn co-transfected with pOG44, Hyg; pulse cells: PB-CMV-TO-rapTEV-teHCV-hcTVMV-tvDiTEV-Neo co-transfected with a plasmid expressing PiggyBac transposase, Gen; EGFRvIII+ cells: PB-CMV-TO-EGFRvIII-IRES-nlsChe co-transfected with a plasmid expressing PiggyBac transposase, Gen. After PiggyBac-based integration, monoclonal cell populations were established through limiting dilution, and preliminary screening was performed to identify clones with highest transgene expression (based on GFP that serves as the scaffold in iTEV, and mCherry that's co-expressed with EGFRvIII), which were used in subsequent experiments. Among the pulse cell clones with highest GFP expression, the one with the least variance was selected. We then subjected this clone to another round of transgenesis (Hyg, CMV-TO-Cer-HO1-FlpIn co-transfected with pOG44) to provide Cerulean as a segmentation marker and heme oxygenase-1 to increase the intracellular concentration of biliverdin that's necessary for enhancing iTEV signal. The final cell line was used in time-lapse imaging.

Time-lapse imaging

For time-lapse imaging of pulse dynamics (Figure 3) monoclonal pulse-generation cells were mixed with parental wild-type HEK293 cells at a 1:10 ratio. Cells were plated on 24-well glass-bottom plates which had been coated with 5 µg/mL with hamster fibronectin for 1 hour at room temperature. Cells were induced with 100 ng/mL doxycyline overnight in normal culturing conditions. The following morning, the media was replaced with imaging media containing FluoroBrite DMEM (Thermo Fisher) supplemented with 10% FBS, 1 mM sodium pyruvate, 1 unit/ml penicillin, 1 µg/ml streptomycin, 2 mM L-glutamine and 1X MEM non-essential amino acids and 100 ng/mL doxycycline.

All time-lapse images were acquired on an inverted Olympus IX81 fluorescence microscope with Zero Drift Control (ZDC), an ASI 2000XY automated stage, iKon-M CCD camera (Andor, Belfast, NIR), and a 60x oil objective (1.42 NA). Fluorophores were excited with an X-Cite XLED1 light source (Lumen Dynamics). Cells were kept in a custom-made environmental chamber enclosing the microscope, with humidified 5% CO2 flow at 37°C. Microscope and image acquisition were controlled by Metamorph software (Molecular Devices).

Imaging started approximately 2 hours after changing the media to fluorescent imaging media. 5 nM rapamycin was added after approximately 2 hours of imaging to induce the pulse. Images were acquired every 20 or 25 min, typically for 20-40 hrs. Cells that were in the field of view before rapamycin induction and remained alive and visible in the field of view without death for at least 20 hours were used for initial data analysis.

For analysis, we only included cells that remained alive throughout the duration of the experiment, remained within the field of view, and had detectable signal/background ratio. IFP fluorescence intensity is dependent on the biliverdin chromophore. Addition of exogenous biliverdin increases IFP fluorescence but also produces IFP-independent background fluorescence. For the movies, to minimize background, we omitted biliverdin from the media, relying instead on lower concentrations produced endogenously. Under these conditions, IFP excitation illumination levels caused some phototoxicity, resulting in a subpopulation of ~50% of cells that died within ~7 hours. The remaining cells continued active division until the end of the movie, or until exit from the field of view. These cells exhibited a range of IFP fluorescence levels overlapping background. 30-60% of these cells in which IFP fluorescence exceeded background. About half of this set had morphologies that were amenable to image-based segmentation and therefore were analyzed further. Within this group, we verified that the circuit dynamics were independent of expression level, as measured by peak IFP fluorescence, suggesting that circuit dynamics are not influenced by expression level within this range.

Movie analysis

Matlab-based single-cell tracking and image normalization software was developed in-house by Yaron Antebi.

Single-cell tracking and image normalization:

Single-cell tracking and image normalization procedures were performed as previously described (*70*) with a few modifications. Briefly, cells constitutively express cytoplasmic Cerulean as a segmentation marker. Due to the diffuse and weak Cerulean signal, manual segmentation was frequently required and cell boundaries were identified in part by phase contrast and GFP fluorescence images (GFP is the protein identified as the "split scaffold" in Figure 3E. It serves a structural role in the context of the IFP reporter, but also fluoresces).

We performed image correction to account and correct for non-uniform illumination as well as background. We assumed a time-independent spatially inhomogeneous illumination profile that is characteristic of the optical path, $I(x, y)$. This was extracted by fitting the low intensity "non-

cell" pixels in the images with a two dimensional paraboloid. In addition we considered two sources of background fluorescence: First, the detector produces a basal pixel value even in the absence of light. This value, denoted B, is spatially homogeneous and time-independent. Second, we considered the autofluorescence of the media. This background source changes over time, and exhibits a spatial profile proportional to the illumination profile, $A(t) * I(x, y)$. With these assumptions, we extracted the corrected fluorescence value using the following equation:

$$F_{corrected}(x, y, t) = \frac{F_{raw}(x, y, t) - B}{I(x, y)} - A(t)$$

For generating the supplementary movie, mean intensities < 5% were set to zero and mean intensities > 99.5% were set to maximum pixel values to limit the effect of extreme pixel values due to noise on image brightness and contrast settings.

Quantification of amplitude and pulse decay:

Data processing: The amplitude and pulse decay calculations were based on total levels of fluorescence in the IFP fluorescent channel. To systematically quantify the fluorescent signal in the IFP channel, total IFP signal intensity $IFP(x, y, t)$ was normalized by the total constitutive Cerulean signal $CFP(x, y, t)$ and rescaled with a baseline variable (90th percentile of $\frac{IFP(x,y,t)}{CFP(x,y,t)}$ at all x positions.) To capture the pulse of IFP signal and avoid distortion of the peak shape, the resulting data was smoothed with a Savitzky-Golay filter using a 3rd order polynomial and a window length of 9. After smoothing, the data were interpolated to equidistant timepoints of 20 minute intervals (Fig. 3H).

Fitting: We fit the pulsing dynamics by taking the smoothed and interpolated data and subtracting the minimum value of the normalized signal intensity from each timepoint. Using MATLAB's tfest function, the normalized data were deconvolved with a finite impulse signal and a third-order linear transfer function resulting in the equation:

$$y = a_1 e^{p_1 x(t)} + a_2 e^{p_2 x(t)} + a_3 e^{p_3 x(t)}$$

The resulting fit was used to determine: (1) the location at which the maximal value of IFP occurred and (2) the delay time, τ, after peak signal at which the signal intensity decayed to 50% its maximum value. After determining the peak location and τ, the mean and standard deviation were calculated.

Data and code availability

The datasets generated and analyzed and the computer code used during the current study are available from the corresponding author.

Supplementary Text

Characterization and optimization of HCVP and its reporter.

For HCV protease (HCVP), we adopted a previously described construct in which the protease and its co-peptide are fused to create a more active single chain protease (*38*). This HCVP initially showed more modest regulation than the other proteases, especially for the repressible reporter (Fig. S1D). We reasoned that increasing the protease affinity to its target could improve its regulatory range. Indeed, incorporating a pair of hetero-dimerizing leucine zippers (*39*) in the protease and its target improved regulation (Fig. S1D, right).

Characterization and optimization of circuits that selectively reduce Ras-activating cells

To exclude the possibility that SOS_{CA} cells are generally more sensitive to Casp3 activation, we first analyzed constitutively dimerized split TEVP variants, one using leucine zippers, and the other adopting a RasG12V mutant that binds constitutively to RBD (*73*) (Fig. S5E). When co-transfected with the TEVP-activatable Casp3, these control constructs displayed no selectivity for SOS_{CA} cells (Fig. S5E), indicating that the regulated Ras-RBD interaction is necessary for the selectivity observed in the main text (Fig. 4C).

To assess the contribution of each additional regulatory interaction in the full circuit, we systematically removed them one at a time, and compared their effects on control and SOS_{CA} cells to the full circuit. Removal of Casp3 inhibition by TVMVP re-introduced substantial reduction in control cells (Fig. S6A, left), and removal of TVMVP inhibition by RasTEVP increased survival in SOS_{CA} cells (Fig. S6A, middle). By contrast, removal of RasTEVP inhibition by TVMVP had no effect on survival in either control or SOS_{CA} cells (Fig. S6A, right). These results indicate that Arms 3,4 (Figs. S5A, S6A) are major contributors to full circuit performance.

For single-transcript delivery of the full circuit, we interposed a wild type internal ribosome entry site (IRES) between Casp3 and RasTEVP coding sequences, followed by one of several IRES variant sequences (*61*) and then the TVMVP (Fig. S6B). Inspired by TVMVP titration results (Fig. S5G), we chose variants with ~30% and ~70% of wild-type strength for the second IRES (*55*), and found that the circuit functioned optimally with the ~70% IRES (Fig. S6B).

Response of RasTEVP to EGF stimulation

To assess the response of RasTEVP to a physiological ligand that normally activates the Ras pathway, we stimulated cells expressing either RasTEVP or constitutively dimerized and membrane-localized TEVP (negative control TEVP) with epidermal growth factor (EGF). When co-transfected with a membrane-localized iTEV reporter, the control construct TEVP-mts exhibited minimal response to EGF stimulation, whereas RasTEVP displayed a modest response to EGF (Fig. S5C).

Comparison of protease-protease and transcriptional regulatory dynamics

In this supplementary section, we use a minimal model to address the question of how a simple transcription factor regulatory step differs in dynamics from a simple protease regulatory step. To make a controlled comparison between the two kinds of regulation, we assume that shared biochemical parameters, such as protein degradation rates, are similar in the two systems. The main conclusion is that protease regulation can occur more rapidly than transcriptional regulation but with timescales that depend on the direction of regulation. By contrast, transcriptional regulation is expected to be slower but show similar timescales in both directions of regulation. While we have considered typical biochemical parameter values here, we note that additional features of any specific system, including feedback structure, could impact their dynamic behavior. Additionally, the quantitative values of the resulting timescales in general depend on the specific choice of biochemical parameter values.

Protease-protease regulation. We modeled repression of one protease by another through direct cleavage, based on the scheme in Fig 1E. We assume the concentration of the input protease, denoted P_0, is maintained at a constant level, with its activity controlled by a small molecule input, as in the scheme of Fig 3E. The output protease, denoted P, is produced at a constant rate A, and undergoes first-order degradation with rate γ_p. The input protease cleaves the output protease at a single cleavage site, converting it to a cleaved form, whose concentration is denoted P_c, with a cleavage rate constant k. The cleaved protease irreversibly dissociates at rate k_d, and undergoes first-order degradation with rate γ_p for a total rate of elimination of $\gamma_p + k_d$. We assume a single cleavage for simplicity, but the same conclusions hold true for two independent cleavage sites, cleavage of either of which is sufficient to inactivate the output protease.

The reactions in the protease-protease model are as follows, where ϕ denotes 'nothing':

1. Synthesis of the output protease: $\phi \xrightarrow{A} P$
2. Degradation of the output protease: $P \xrightarrow{\gamma_p} \phi$
3. Catalytic cleavage of the output protease: $P_0 + P \xrightarrow{k} P_0 + P_c$
4. Dissociation of the cleaved protease: $P_c \xrightarrow{k_d} \phi$
5. Degradation of the cleaved protease: $P_c \xrightarrow{\gamma_p} \phi$

Assuming protease cleavage functions in a linear regime far from saturation, consistent with published K_m values *(23)* and our bandpass modeling, the reaction can be expressed as a set of ordinary differential equations (ODEs):

$$\frac{dP}{dt} = A - kP_0P - \gamma_pP$$
$$\frac{dP_c}{dt} = kP_0P - P_c\left(k_d + \gamma_p\right)$$

Because the absolute value of the production rate A does not affect the dynamics of the system, we arbitrarily set its value to 1 Mh^{-1}. For the dissociation rate, we assumed $k_d = 5h^{-1}$ based on indirect measurements *(71)*. For the protein degradation rate, we assumed a biologically realistic value of $\gamma_p = 0.1h^{-1}$.

Based on our bandpass fits (Figs. 3B-D, Methods), cleavage by a protease, when the input protease activity is high, occurs at a rate comparable to the rate of degron-mediated degradation ($\sim 5h^{-1}$). We also assumed that the OFF input protease is 20-fold less active than the ON state based on the dynamic range observed in Figure 1. (Note that the value of this regulatory range does not affect our conclusions about the timescales of regulation.) Finally, we assumed the small-molecule-induced ON-OFF switch reaches steady-state much faster than the other reactions, so that the cleavage term can be approximated by a step function, taking one of two possible values:

$kP_0 = 0.25\ h^{-1}\ (input\ OFF)$ or $5\ h^{-1}\ (input\ ON)$

To simulate output dynamics in response to changes in the input, we first set the input protease to ON, and the output protease to its steady state value of $P + P_c$. At t=10h, we switched the input to OFF and simulated the equations for 70h (10-80h). Finally, we switched the input back to ON and simulated another 70h (80h-150h). In Fig. S7, we plot the resulting dynamics of the output protease, normalized to its maximum value. Note the asymmetric response time, which is faster for input OFF→ON switch than ON→OFF ($t_{\frac{1}{2}}$ = 0.32 h^{-1} vs. 2.3 h^{-1}).

Transcriptional regulation. As a comparison to protease regulation, we modeled a logically equivalent transcriptional repression step. The input transcription factor was maintained at a constant concentration of T_0, with its activity assumed to be controlled by a small molecule, as with the protease. The input transcription factor regulates the output mRNA, T_m, whose production follows a standard rate law: $\frac{K}{K+T_0}A_m$. T_m undergoes first-order degradation with rate γ_m. The output protein T_p is translated from the mRNA at rate A_p, and degraded with rate γ_p. The reactions are as follows:

1. mRNA synthesis: $\phi \xrightarrow{\frac{K}{K+T_0}A_m} T_m$
2. mRNA degradation: $T_m \xrightarrow{\gamma_m} \phi$
3. protein synthesis: $T_m \xrightarrow{A_p} T_m + T_p$
4. protein degradation: $T_p \xrightarrow{\gamma_p} \phi$

These reactions can be converted to ODEs for each of the components:

$$\frac{dT_m}{dt} = \frac{K}{K+T_0}A_m - \gamma_m T_m$$

$$\frac{dT_p}{dt} = A_p T_m - \gamma_p T_p$$

Without loss of generality we set the production rate $A_m = 1\ Mh^{-1}$ and $A_p = 1\ h^{-1}$. We used the same protein degradation rate as in the protease regulation case above: $\gamma_p = 0.1h^{-1}$. For mRNA degradation, we simulate two values at opposite extremes of the biological range for mammalian mRNA *(72)*:$\gamma_m = 0.1h^{-1}$ (more stable), and $5h^{-1}$ (less stable). As above, we also

assumed that the small-molecule-controlled input ON-OFF switch is much faster than the other reactions. To match the protease conditions, we assumed T_0 also undergoes a 20-fold regulation, from $T_0 = 0.5K$ $(input\ OFF)$ to $10K$ $(input\ ON)$, although we note that the exact dynamic range of T_0 or the exact choice of the Hill function does not affect output dynamics.

We simulated this simple model of transcriptional regulation with fast and slow mRNA degradation rates, following the same ON → OFF → ON input temporal profile used in the protease regulation case. To focus on the timescale of regulation, we normalized each curve to its maximal value. For transcriptional regulation, $t_{\frac{1}{2}}$ = 7.2 h^{-1} and 17 h^{-1} for fast and slow mRNA decay, respectively, regardless whether the input undergoes ON→OFF or OFF→ON switch. When input switches from ON to OFF, protease and transcriptional regulation occurs on comparable timescales, although their difference is more apparent in the slower mRNA degradation case. When input switches from OFF to ON, however, protease regulation generates a much faster response time compared to transcriptional regulation and the ON to OFF switch in the protease regulation case (Fig. S7). Intuitively, the dynamics of each process is limited by the slowest rate at which a species decays, which is the relatively slow protein degradation rate for transcriptional control (or both protein and mRNA degradation rates when mRNA is more stable); in contrast, the output protease decays at a much faster rate because, in addition to regular protein degradation, it is also cleaved by input protease, and the rate is even higher when the input is switched to its active state.

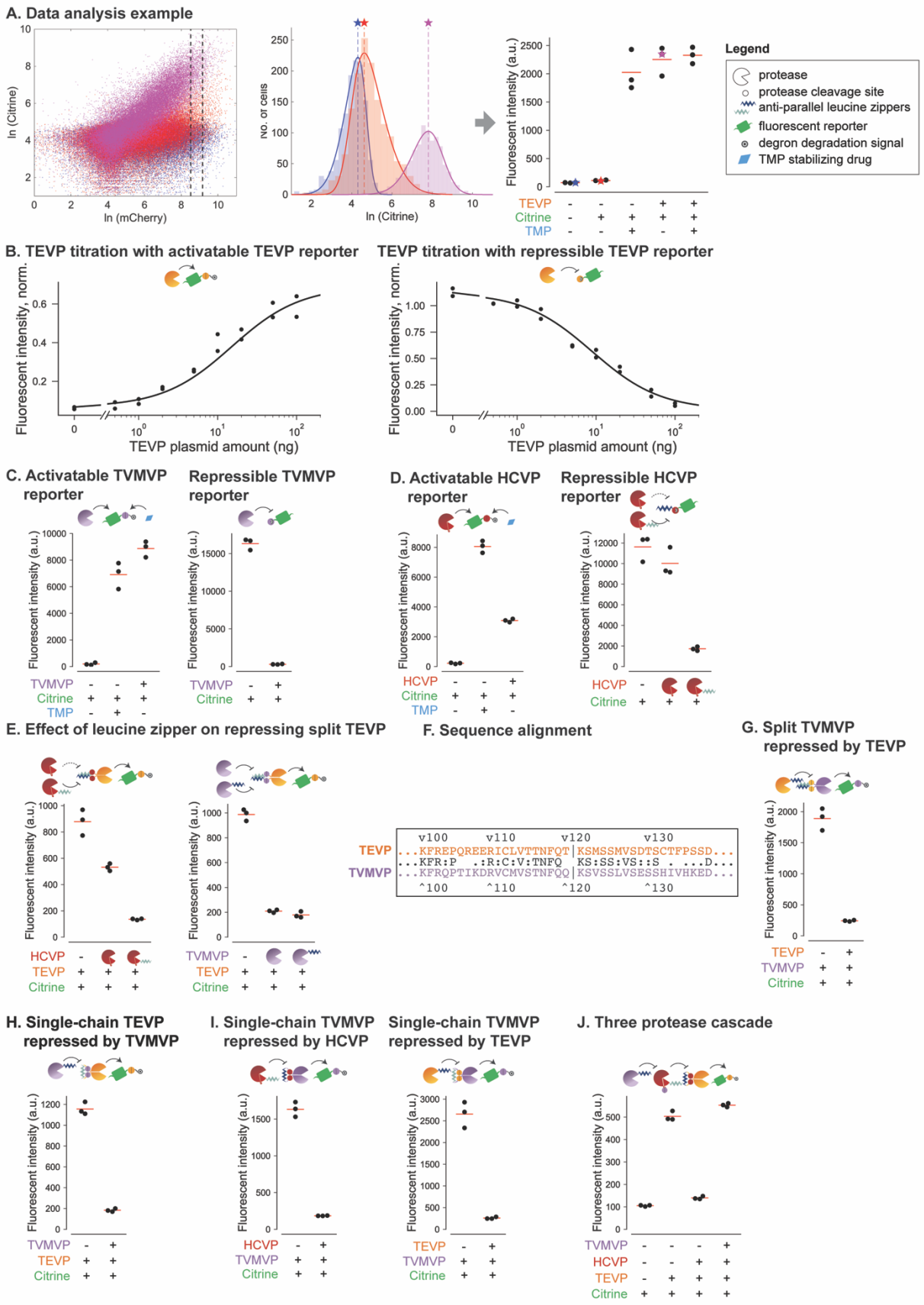
A. Data analysis example
ln (Citrine)
ln (mCherry)
No. of cells
ln (Citrine)
Fluorescent intensity (a.u.)
TEVP
Citrine
TMP
Legend
protease
protease cleavage site
anti-parallel leucine zippers
fluorescent reporter
degron degradation signal
TMP stabilizing drug
B. TEVP titration with activatable TEVP reporter
TEVP titration with repressible TEVP reporter
Fluorescent intensity, norm.
TEVP plasmid amount (ng)
C. Activatable TVMVP reporter
Repressible TVMVP reporter
D. Activatable HCVP reporter
Repressible HCVP reporter
TVMVP
HCVP
E. Effect of leucine zipper on repressing split TEVP
F. Sequence alignment
v100 v110 v120 v130
TEVP ...KFREPQREERICLVTTNFQT|KSMSSMVSDTSCTFPSSD...
...KFR:P .:R:C:V:TNFQ KS:SS:VS::S . ...D...
TVMVP ...KFRQPTIKDRVCMVSTNFQQ|KSVSSLVSESSHIVHKED...
^100 ^110 ^120 ^130
G. Split TVMVP repressed by TEVP
H. Single-chain TEVP repressed by TVMVP
I. Single-chain TVMVP repressed by HCVP
Single-chain TVMVP repressed by TEVP
J. Three protease cascade

Figure S1 | Characterization and optimization of CHOMP components. A, Three representative log-log flow cytometry scatter plots showing autofluorescence (blue) as well as reporter co-transfected with (purple) and without (orange) TEVP. Citrine signal is represented on the y-axis and the co-transfection marker mCherry on the x-axis. Dashed lines indicate the gate on mCherry expression analyzed in Fig. 1B. The histograms and data points are the same as in Fig. 1B, except for the additionally displayed autofluorescence distribution. **B,** Dose-response curves for activatable (left) and repressible (right) TEVP reporters (indicated schematically above each plot). The solid lines are fits based on the same equations as those used in bandpass analysis. **C,D,** Reporters activatable (left) and repressible (right) by TVMVP (**C**) and HCVP (**D**). The designs are identical to those of the TEVP reporters with two exceptions: First, the specific cleavage site sequences have been replaced with those of the regulatory protease. Second, the repressible HCVP reporter contains an additional leucine zipper compared to the other constructs, and it exhibits stronger repression when HCVP is tagged with the complementary leucine zipper (both shown in schematic, right-hand side of (**D**). **E,** Incorporating a leucine zipper (zig-zag) on HCVP (left) enhances repression of TEVP but has minimal effects when used on TVMVP (right). **F,** Alignment of TEVP and TVMVP sequences enables identification of TVMVP split site (vertical bars). **G,** A similar design enables repression of split TVMVP by TEVP. **H,** TVMVP can repress a single-chain TEVP. **I,** The single-chain TVMVP is repressed by HCVP (left) and TEVP (right). **J,** An alternative three protease cascade, distinct from that in Fig. 1G, can also propagate signals.

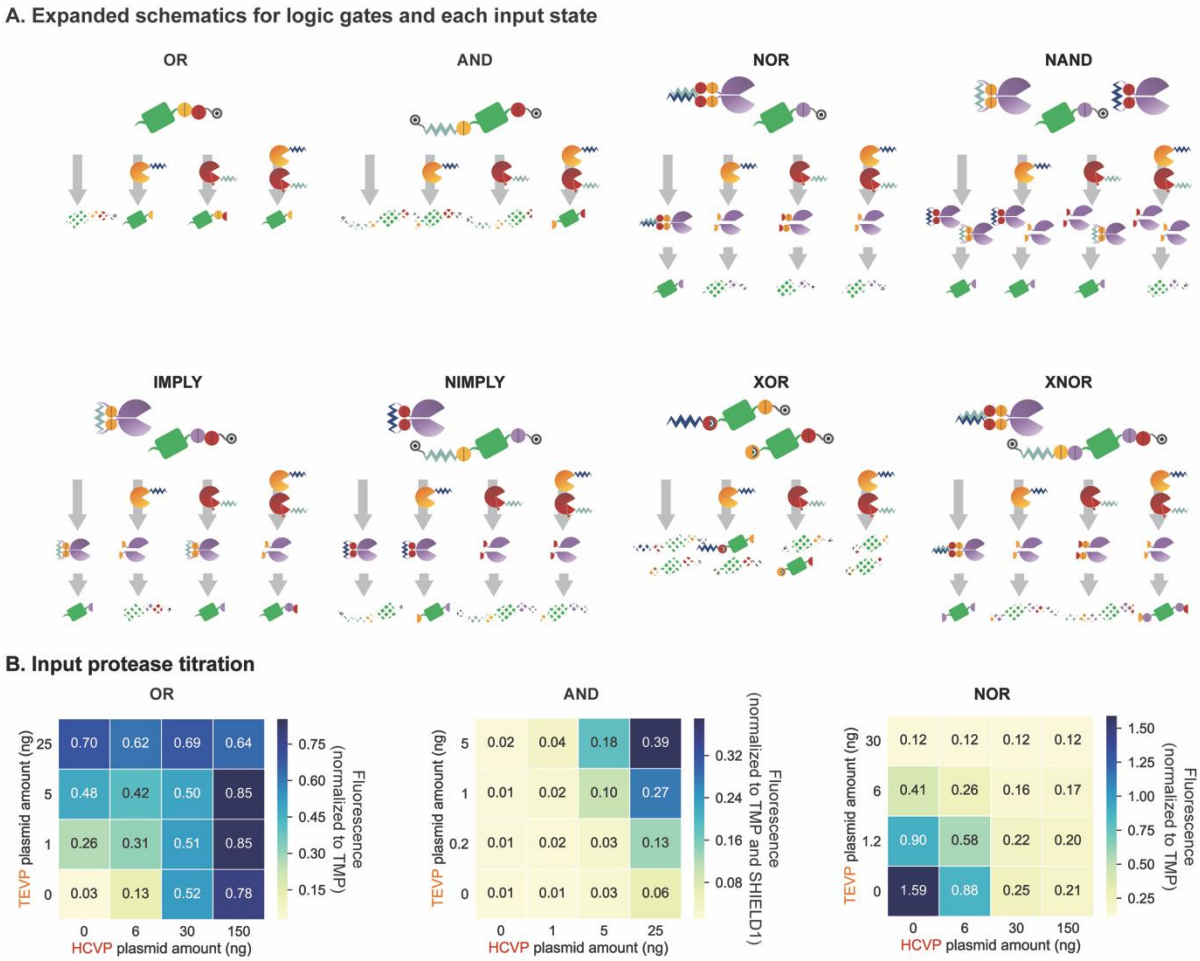
A. Expanded schematics for logic gates and each input state
OR
AND
NOR
NAND
IMPLY
NIMPLY
XOR
XNOR
B. Input protease titration
OR
TEVP plasmid amount (ng)
25 0.70 0.62 0.69 0.64
5 0.48 0.42 0.50 0.85
1 0.26 0.31 0.51 0.85
0 0.03 0.13 0.52 0.78
0 6 30 150
HCVP plasmid amount (ng)
0.75 0.60 0.45 0.30 0.15
Fluorescence (normalized to TMP)
AND
TEVP plasmid amount (ng)
5 0.02 0.04 0.18 0.39
1 0.01 0.02 0.10 0.27
0.2 0.01 0.02 0.03 0.13
0 0.01 0.01 0.03 0.06
0 1 5 25
HCVP plasmid amount (ng)
0.32 0.24 0.16 0.08
Fluorescence (normalized to TMP and SHIELD1)
NOR
TEVP plasmid amount (ng)
30 0.12 0.12 0.12 0.12
6 0.41 0.26 0.16 0.17
1.2 0.90 0.58 0.22 0.20
0 1.59 0.88 0.25 0.21
0 6 30 150
HCVP plasmid amount (ng)
1.50 1.25 1.00 0.75 0.50 0.25
Fluorescence (normalized to TMP)
C. Reporter titration
OR: 30 ng
AND: 30 ng
NOR: 30 ng
OR: 150 ng
AND: 150 ng
NOR: 150 ng
Fluorescent intensity, norm.
Fluorescent intensity (a.u.)
TEVP 0 1 0 1
HCVP 0 0 1 1

Figure S2 | Expanded schematics for logic gates and characterization of OR, AND, and NOR logic gates. A, Expanded schematic diagrams of logic gates for each input state. For each gate, the corresponding diagram is shown on top, followed by the expected behavior in each of the four input states, with or without TEVP (yellow) and HCVP (red). The presence of Citrine (green) indicates the "ON" output state, while degraded Citrine (shown as chopped up reporter) represents the "OFF" state. **B,** Responses of logic gates across 16 input concentration combinations for OR, AND, and NOR gates. Fluorescent intensities are normalized to the corresponding reporter stabilized with TMP (OR and NOR) or TMP and SHIELD1 (AND). In each case, reporter was used at a concentration of 150 ng. **C,** Varying reporter expression levels by transfecting OR, AND, and NOR reporter plasmids at 30 ng and 150 ng. Left axis displays fluorescent intensity values normalized to reporter stabilized with TMP or TMP and SHIELD1. Inputs TEVP and HCVP at 150 ng each. Right axis shows raw fluorescent intensity values.

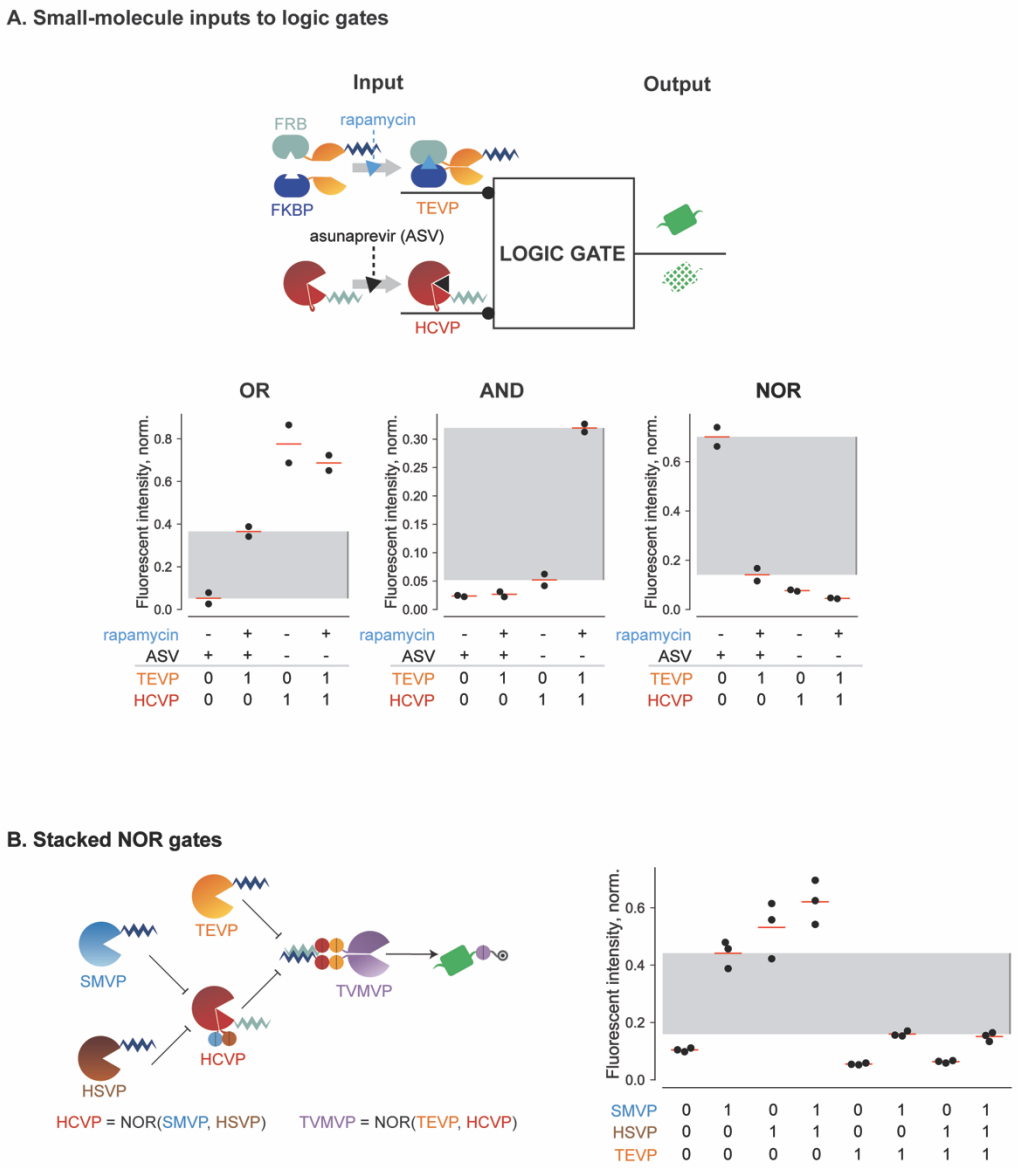

Figure S3 | Expanding the inputs and complexity of logic gates. A, Characterization of OR, AND, and NOR gates using small molecule inputs. Asunaprevir (ASV), an inhibitor of HCVP and rapamycin, a chemical inducer of dimerization of a FRB/FKBP and thereby an inducer of split TEVP, were used as inputs. Each plot shows the output behavior in the presence or absence of each of the two small molecule inputs. The expected presence or absence of input protease activities is shown below the inducer rows. **B,** NOR gates can be composed. Left, diagram of nested NOR gate. Soybean mosaic virus protease (SMVP) and herpes simplex virus Protease (HSVP) are inputs to HCVP activity. HCVP and TEVP are, in turn, inputs to TVMVP. Finally, TVMVP stabilizes the Citrine reporter. Right, performance of the nested NOR gate with protease inputs SMBVP, HSVP, and TEVP indicated in graph. SMVP at 80 ng, HSVP at 150 ng, TEVP at 30 ng, HCVP at 100 ng, and TVMVP at 100 ng.

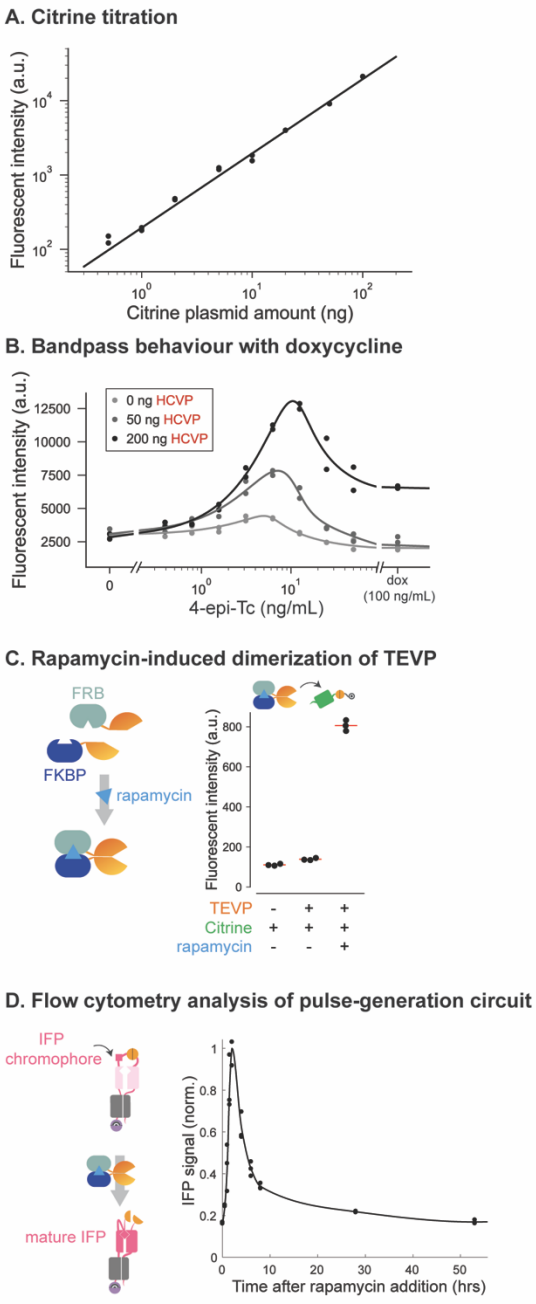

Figure S4 | Characterization of bandpass and pulse-generation circuits. **A,** Linear correlation between the amount of transfected DNA and Citrine expression from CMV promoter. **B**, Bandpass behavior in response to TEVP and TVMVP expressed at constant DNA concentration but with different levels of induction by tetracycline analog 4-epi-Tc, x-axis). **C**, A TEVP variant activated by rapamycin-mediated dimerization of FKBP and FRB domains exhibits rapamycin-dependent activation. **D**, Left, diagram for activation of the IFP reporter by TEVP cleavage. Right, flow cytometry analysis of the dynamics of the pulse generation circuit (also see Figs. 3E,F for diagrams). Each dot represents the mode of the reporter fluorescence distribution at each time point. These data were obtained with the same stable cell line as in Fig. 3H.

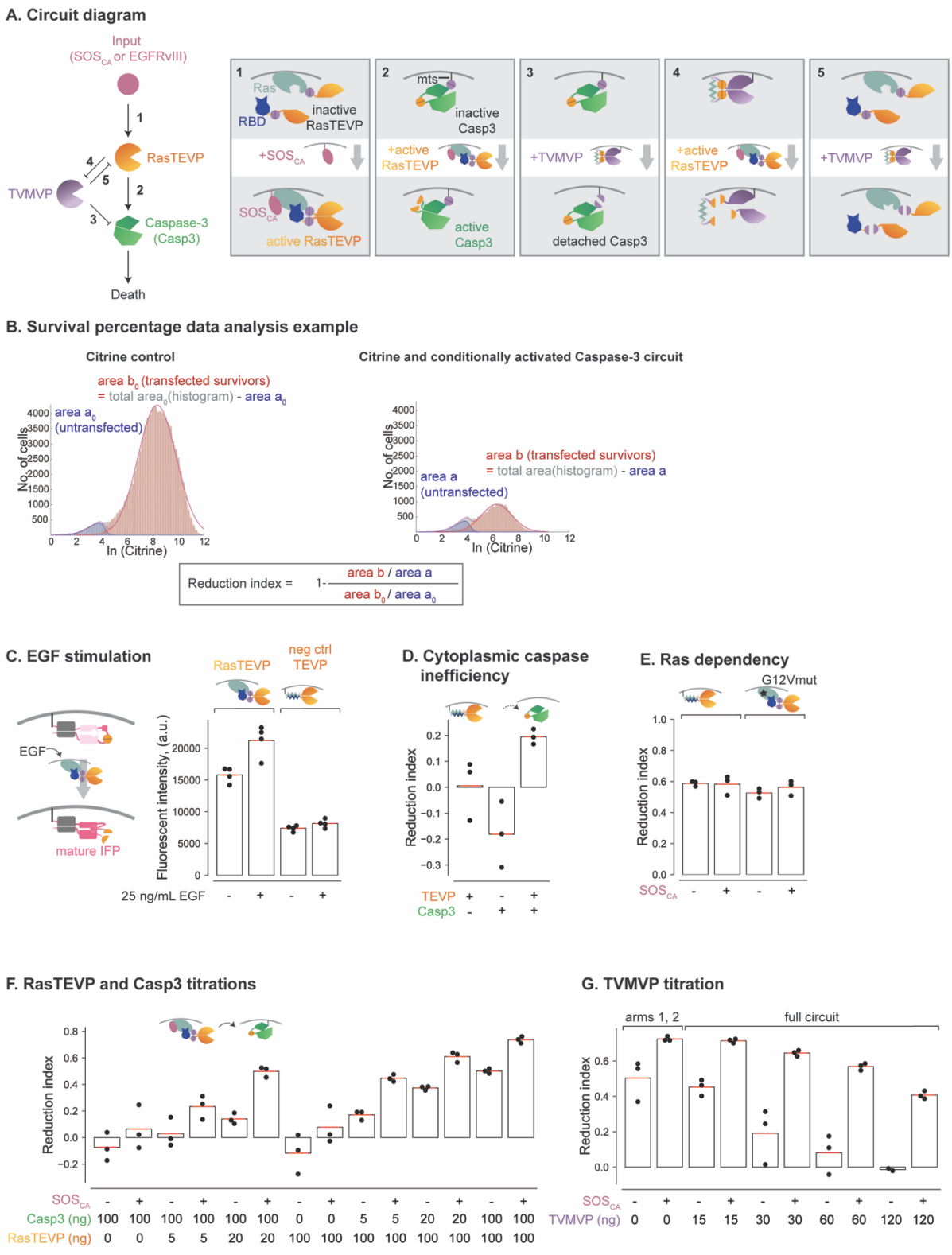

Figure S5 | Characterization and optimization of circuits that selectively activate Casp3 in response to Ras activation. A, Expanded schematic diagram of the full circuit and each of its regulatory interactions (numbered arrows and corresponding boxes). **B**, Example of reduction

index analysis. The reduction index is calculated by comparing the number of surviving transfected cells in experimental vs. Citrine-only conditions, normalized to their respective untransfected populations, as shown in the equation. See also Methods for more details. Blue and red dashed lines indicate individual Gaussian distributions in the two-component fit, and purple dashed line indicates their sum. Blue shaded area is the area beneath the blue dashed line, and red shaded area is total area (grey histogram) minus blue shaded area (*not* the area beneath the red dashed line). **C**, Response of RasTEVP to physiological ligand epidermal growth factor, EGF. Left, diagram for activation of the membrane-localized IFP reporter (same as iTEV used in the pulse circuit (Fig. 3E) but with an additional 12 amino-acid N-terminal signal peptide from Lyn for membrane localization) by RasTEVP cleavage upon EGF stimulation. Right, co-transfection of iTEV reporter and RasTEVP or constitutively dimerized membrane-localized TEVP ('neg ctrl TEVP'). Left two bars show RasTEVP activation in response to EGF. Right two bars show negative control TEVP's relatively lower response to EGF stimulation. These transfections included 25 ng of RasTEVP and 5 ng each for the negative control TEVP components. EGF was used at 25 ng/mL. **D,** Cytoplasmic TEVP-activatable Casp3 causes limited reduction of cell number in the presence of membrane-localized TEVP reconstituted through leucine zippers (compare to Fig. 4B). **E**, Reduction index is unaffected by SOS_{CA} status in the presence of constitutive Casp3 activation with no Ras-dependent regulation (Casp3 not depicted). For the left bars, TEVP is constitutively active through the membrane-tethered leucine zippers. The right bars uses a G12V mutation in Ras that renders it constitutively active (*65*). **F,** The effects of RasTEVP and Casp3 doses on reduction index. Each bar represents the reduction indices from indicated concentrations of RasTEVP and Casp3 plasmids in control or SOS_{CA} cells. **G**, Dose of TVMVP tunes the circuit's selectivity for SOS_{CA} cells (the first and fourth pairs of bars also shown in Fig. 4C). 90 ng of RasTEVP and Casp3 were transfected in each case.

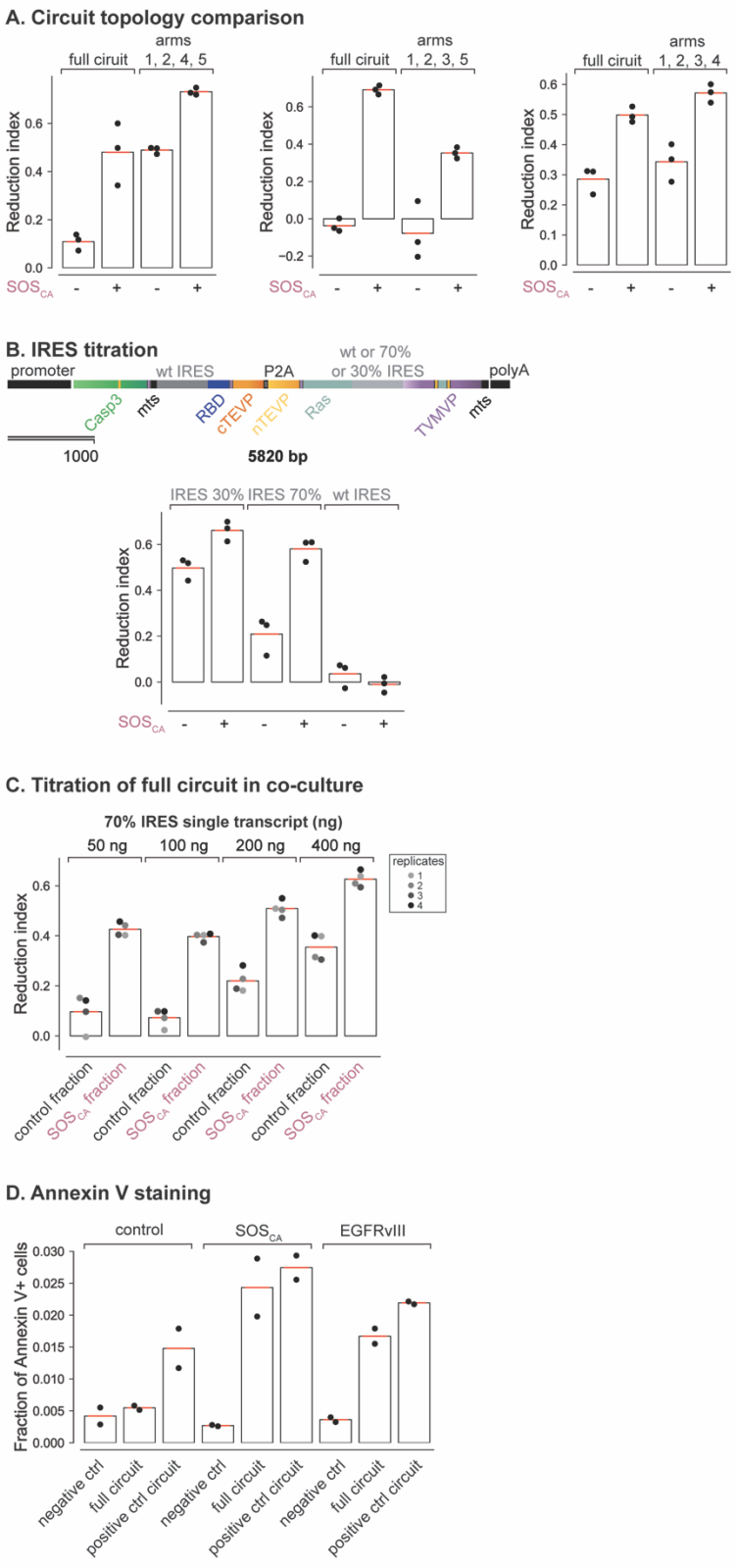

Figure S6 | Further characterization and optimization of circuits that selectively activate Casp3 in response to Ras activation. A, Analysis of contributions of individual regulatory edges in panel **S5A** to overall selectivity. Left, removing TVMVP ⊣ Casp3 (Arm 3) increases reduction index for both control and SOS_{CA} cells; middle, removing RasTEVP ⊣ TVMVP (Arm 4) decreases reduction in SOS_{CA} cells; right, removing TVMVP ⊣ RasTEVP (Arm 5) has no significant effect. We also note that, despite the qualitatively consistent selectivity, there is quantitative day-to-day variability. **B**, IRES variants with reported strengths of 30% and 70% of wild-type strength can be used to optimize TVMVP expression level in a single transcript. The IRES variant reported to express at ~70% level of wild type (*61*) balances survival of control cells and reduction of SOS_{CA} cells. 200 ng for each single-transcript variant. **C**, Optimizing transfection dose for full single-transcript circuit with 70% IRES. Each pair of bars represents 4 replicate co-cultures (gray dots) of control and SOS_{CA} cells transfected with the indicated amount of the single-transcript circuit. **D,** Annexin V staining of control, SOS_{CA} and EGFRvIII+ cells. Transfection of a negative control, full circuit and the positive control circuit from Fig 4D into each cell line at 50 ng each. We note that the fraction of apoptotic cells in all conditions

are smaller than what would be indicated by reduction index, as expected due to heterogeneity in the timing of initiation of apoptosis and the loss of Annexin-V+ cells due to cell death. The two effects together cause any given time window to capture only a fraction of the cumulative number of Annexin-V+ cells over the whole time-course.

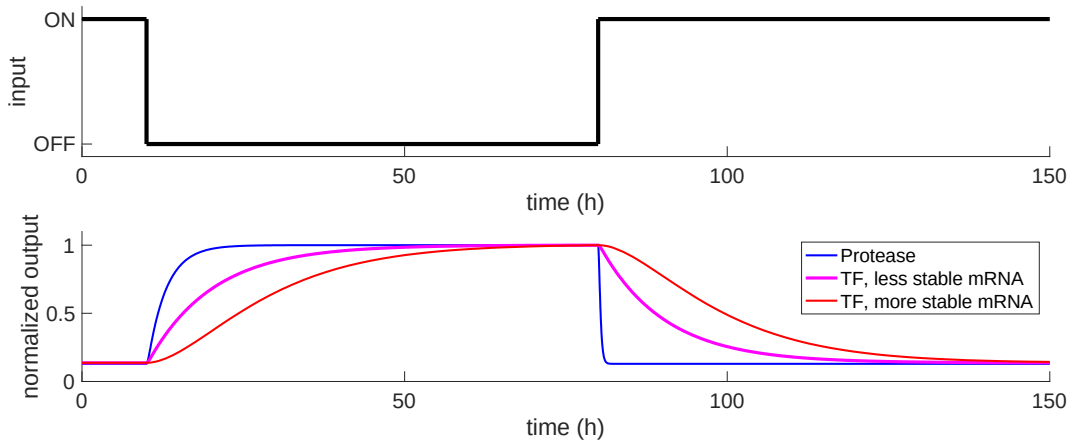

Figure S7. Simulated protease-protease and TF-TF regulation dynamics. This plot compares the dynamic response of protease-protease regulation (blue) and transcriptional regulation (pink and red, representing distinct parameter sets) to step changes in an input protease/TF (black line). See Supplementary text for models and parameter values.

Table S1. List of plasmids constructed for this study and their use in figures.

Movie S1. Time-lapse movie of four representative cells displaying pulsing signal.

References and Notes

1. J. Bonnet, P. Yin, M. E. Ortiz, P. Subsoontorn, D. Endy, Amplifying genetic logic gates. *Science* **340**, 599–603 (2013). doi:10.1126/science.1232758 Medline

2. B. H. Weinberg, N. T. H. Pham, L. D. Caraballo, T. Lozanoski, A. Engel, S. Bhatia, W. W. Wong, Large-scale design of robust genetic circuits with multiple inputs and outputs for mammalian cells. *Nat. Biotechnol.* **35**, 453–462 (2017). doi:10.1038/nbt.3805 Medline

3. S. Ausländer, D. Ausländer, M. Müller, M. Wieland, M. Fussenegger, Programmable single-cell mammalian biocomputers. *Nature* **487**, 123–127 (2012). doi:10.1038/nature11149 Medline

4. K. Rinaudo, L. Bleris, R. Maddamsetti, S. Subramanian, R. Weiss, Y. Benenson, A universal RNAi-based logic evaluator that operates in mammalian cells. *Nat. Biotechnol.* **25**, 795–801 (2007). doi:10.1038/nbt1307 Medline

5. L. Wroblewska, T. Kitada, K. Endo, V. Siciliano, B. Stillo, H. Saito, R. Weiss, Mammalian synthetic circuits with RNA binding proteins for RNA-only delivery. *Nat. Biotechnol.* **33**, 839–841 (2015). doi:10.1038/nbt.3301 Medline

6. A. S. Khalil, T. K. Lu, C. J. Bashor, C. L. Ramirez, N. C. Pyenson, J. K. Joung, J. J. Collins, A synthetic biology framework for programming eukaryotic transcription functions. *Cell* **150**, 647–658 (2012). doi:10.1016/j.cell.2012.05.045 Medline

7. N. Roquet, A. P. Soleimany, A. C. Ferris, S. Aaronson, T. K. Lu, Synthetic recombinase-based state machines in living cells. *Science* **353**, aad8559 (2016). doi:10.1126/science.aad8559 Medline

8. A. A. K. Nielsen, B. S. Der, J. Shin, P. Vaidyanathan, V. Paralanov, E. A. Strychalski, D. Ross, D. Densmore, C. A. Voigt, Genetic circuit design automation. *Science* **352**, aac7341 (2016). doi:10.1126/science.aac7341 Medline

9. B. Angelici, E. Mailand, B. Haefliger, Y. Benenson, Synthetic Biology Platform for Sensing and Integrating Endogenous Transcriptional Inputs in Mammalian Cells. *Cell Reports* **16**, 2525–2537 (2016). doi:10.1016/j.celrep.2016.07.061 Medline

10. J. J. Lohmueller, T. Z. Armel, P. A. Silver, A tunable zinc finger-based framework for Boolean logic computation in mammalian cells. *Nucleic Acids Res.* **40**, 5180–5187 (2012). doi:10.1093/nar/gks142 Medline

11. I. Budihardjo, H. Oliver, M. Lutter, X. Luo, X. Wang, Biochemical pathways of caspase activation during apoptosis. *Annu. Rev. Cell Dev. Biol.* **15**, 269–290 (1999). doi:10.1146/annurev.cellbio.15.1.269 Medline

12. M. A. Marchisio, J. Stelling, Computational design of synthetic gene circuits with composable parts. *Bioinformatics* **24**, 1903–1910 (2008). doi:10.1093/bioinformatics/btn330 Medline

13. B. J. Yeh, R. J. Rutigliano, A. Deb, D. Bar-Sagi, W. A. Lim, Rewiring cellular morphology pathways with synthetic guanine nucleotide exchange factors. *Nature* **447**, 596–600 (2007). doi:10.1038/nature05851 Medline

14. J. E. Dueber, B. J. Yeh, K. Chak, W. A. Lim, Reprogramming control of an allosteric signaling switch through modular recombination. *Science* **301**, 1904–1908 (2003). doi:10.1126/science.1085945 Medline

15. S.-H. Park, A. Zarrinpar, W. A. Lim, Rewiring MAP kinase pathways using alternative scaffold assembly mechanisms. *Science* **299**, 1061–1064 (2003). doi:10.1126/science.1076979 Medline

16. P. L. Howard, M. C. Chia, S. Del Rizzo, F.-F. Liu, T. Pawson, Redirecting tyrosine kinase signaling to an apoptotic caspase pathway through chimeric adaptor proteins. *Proc. Natl. Acad. Sci. U.S.A.* **100**, 11267–11272 (2003). doi:10.1073/pnas.1934711100 Medline

17. D. M. Barrett, N. Singh, D. L. Porter, S. A. Grupp, C. H. June, Chimeric antigen receptor therapy for cancer. *Annu. Rev. Med.* **65**, 333–347 (2014). doi:10.1146/annurev-med-060512-150254 Medline

18. L. Morsut, K. T. Roybal, X. Xiong, R. M. Gordley, S. M. Coyle, M. Thomson, W. A. Lim, Engineering Customized Cell Sensing and Response Behaviors Using Synthetic Notch Receptors. *Cell* **164**, 780–791 (2016). doi:10.1016/j.cell.2016.01.012 Medline

19. K. T. Roybal, L. J. Rupp, L. Morsut, W. J. Walker, K. A. McNally, J. S. Park, W. A. Lim, Precision Tumor Recognition by T Cells With Combinatorial Antigen-Sensing Circuits. *Cell* **164**, 770–779 (2016). doi:10.1016/j.cell.2016.01.011 Medline

20. V. Stein, M. Nabi, K. Alexandrov, Ultrasensitive Scaffold-Dependent Protease Sensors with Large Dynamic Range. *ACS Synth. Biol.* **6**, 1337–1342 (2017). doi:10.1021/acssynbio.6b00370 Medline

21. V. Stein, K. Alexandrov, Protease-based synthetic sensing and signal amplification. *Proc. Natl. Acad. Sci. U.S.A.* **111**, 15934–15939 (2014). doi:10.1073/pnas.1405220111 Medline

22. J. C. Carrington, W. G. Dougherty, A viral cleavage site cassette: Identification of amino acid sequences required for tobacco etch virus polyprotein processing. *Proc. Natl. Acad. Sci. U.S.A.* **85**, 3391–3395 (1988). doi:10.1073/pnas.85.10.3391 Medline

23. J. Tözsér, J. E. Tropea, S. Cherry, P. Bagossi, T. D. Copeland, A. Wlodawer, D. S. Waugh, Comparison of the substrate specificity of two potyvirus proteases. *FEBS J.* **272**, 514–523 (2005). doi:10.1111/j.1742-4658.2004.04493.x Medline

24. R. Bartenschlager, The NS3/4A proteinase of the hepatitis C virus: Unravelling structure and function of an unusual enzyme and a prime target for antiviral therapy. *J. Viral Hepat.* **6**, 165–181 (1999). doi:10.1046/j.1365-2893.1999.00152.x Medline

25. M. J. Adams, J. F. Antoniw, F. Beaudoin, Overview and analysis of the polyprotein cleavage sites in the family Potyviridae. *Mol. Plant Pathol.* **6**, 471–487 (2005). doi:10.1111/j.1364-3703.2005.00296.x Medline

26. C. Taxis, G. Stier, R. Spadaccini, M. Knop, Efficient protein depletion by genetically controlled deprotection of a dormant N-degron. *Mol. Syst. Biol.* **5**, 267 (2009). doi:10.1038/msb.2009.25 Medline

27. M. T. Butko, J. Yang, Y. Geng, H. J. Kim, N. L. Jeon, X. Shu, M. R. Mackey, M. H. Ellisman, R. Y. Tsien, M. Z. Lin, Fluorescent and photo-oxidizing TimeSTAMP tags

track protein fates in light and electron microscopy. *Nat. Neurosci.* **15**, 1742–1751 (2012). doi:10.1038/nn.3246 Medline

28. H. K. Chung, C. L. Jacobs, Y. Huo, J. Yang, S. A. Krumm, R. K. Plemper, R. Y. Tsien, M. Z. Lin, Tunable and reversible drug control of protein production via a self-excising degron. *Nat. Chem. Biol.* **11**, 713–720 (2015). doi:10.1038/nchembio.1869 Medline

29. J. Fernandez-Rodriguez, C. A. Voigt, Post-translational control of genetic circuits using Potyvirus proteases. *Nucleic Acids Res.* **44**, 6493–6502 (2016). doi:10.1093/nar/gkw537 Medline

30. N. H. Kipniss, P. C. D. P. Dingal, T. R. Abbott, Y. Gao, H. Wang, A. A. Dominguez, L. Labanieh, L. S. Qi, Engineering cell sensing and responses using a GPCR-coupled CRISPR-Cas system. *Nat. Commun.* **8**, 2212 (2017). doi:10.1038/s41467-017-02075-1 Medline

31. G. Barnea, W. Strapps, G. Herrada, Y. Berman, J. Ong, B. Kloss, R. Axel, K. J. Lee, The genetic design of signaling cascades to record receptor activation. *Proc. Natl. Acad. Sci. U.S.A.* **105**, 64–69 (2008). doi:10.1073/pnas.0710487105 Medline

32. N. M. Daringer, R. M. Dudek, K. A. Schwarz, J. N. Leonard, Modular extracellular sensor architecture for engineering mammalian cell-based devices. *ACS Synth. Biol.* **3**, 892–902 (2014). doi:10.1021/sb400128g Medline

33. J. A. Gramespacher, A. J. Stevens, D. P. Nguyen, J. W. Chin, T. W. Muir, Intein Zymogens: Conditional Assembly and Splicing of Split Inteins via Targeted Proteolysis. *J. Am. Chem. Soc.* **139**, 8074–8077 (2017). doi:10.1021/jacs.7b02618 Medline

34. D. S. Waugh, An overview of enzymatic reagents for the removal of affinity tags. *Protein Expr. Purif.* **80**, 283–293 (2011). doi:10.1016/j.pep.2011.08.005 Medline

35. M. Iwamoto, T. Björklund, C. Lundberg, D. Kirik, T. J. Wandless, A general chemical method to regulate protein stability in the mammalian central nervous system. *Chem. Biol.* **17**, 981–988 (2010). doi:10.1016/j.chembiol.2010.07.009 Medline

36. A. Varshavsky, The N-end rule: Functions, mysteries, uses. *Proc. Natl. Acad. Sci. U.S.A.* **93**, 12142–12149 (1996). doi:10.1073/pnas.93.22.12142 Medline

37. S. Nallamsetty, R. B. Kapust, J. Tözsér, S. Cherry, J. E. Tropea, T. D. Copeland, D. S. Waugh, Efficient site-specific processing of fusion proteins by tobacco vein mottling virus protease in vivo and in vitro. *Protein Expr. Purif.* **38**, 108–115 (2004). doi:10.1016/j.pep.2004.08.016 Medline

38. S. S. Taremi, B. Beyer, M. Maher, N. Yao, W. Prosise, P. C. Weber, B. A. Malcolm, Construction, expression, and characterization of a novel fully activated recombinant single-chain hepatitis C virus protease. *Protein Sci.* **7**, 2143–2149 (1998). doi:10.1002/pro.5560071011 Medline

39. I. Ghosh, A. D. Hamilton, L. Regan, Antiparallel Leucine Zipper-Directed Protein Reassembly: Application to the Green Fluorescent Protein. *J. Am. Chem. Soc.* **122**, 5658–5659 (2000). doi:10.1021/ja994421w

40. M. C. Wehr, R. Laage, U. Bolz, T. M. Fischer, S. Grünewald, S. Scheek, A. Bach, K.-A. Nave, M. J. Rossner, Monitoring regulated protein-protein interactions using split TEV. *Nat. Methods* **3**, 985–993 (2006). doi:10.1038/nmeth967 Medline

41. L. A. Banaszynski, L.-C. Chen, L. A. Maynard-Smith, A. G. L. Ooi, T. J. Wandless, A rapid, reversible, and tunable method to regulate protein function in living cells using synthetic small molecules. *Cell* **126**, 995–1004 (2006). doi:10.1016/j.cell.2006.07.025 Medline

42. F. Rossi, C. A. Charlton, H. M. Blau, Monitoring protein-protein interactions in intact eukaryotic cells by beta-galactosidase complementation. *Proc. Natl. Acad. Sci. U.S.A.* **94**, 8405–8410 (1997). doi:10.1073/pnas.94.16.8405 Medline

43. S. A. Ghabrial, H. A. Smith, T. D. Parks, W. G. Dougherty, Molecular genetic analyses of the soybean mosaic virus NIa proteinase. *J. Gen. Virol.* **71**, 1921–1927 (1990). doi:10.1099/0022-1317-71-9-1921 Medline

44. S. P. Weinheimer, P. J. McCann 3rd, D. R. O'Boyle 2nd, J. T. Stevens, B. A. Boyd, D. A. Drier, G. A. Yamanaka, C. L. DiIanni, I. C. Deckman, M. G. Cordingley, Autoproteolysis of herpes simplex virus type 1 protease releases an active catalytic domain found in intermediate capsid particles. *J. Virol.* **67**, 5813–5822 (1993). Medline

45. Y. Hart, U. Alon, The utility of paradoxical components in biological circuits. *Mol. Cell* **49**, 213–221 (2013). doi:10.1016/j.molcel.2013.01.004 Medline

46. A. Porcher, N. Dostatni, The bicoid morphogen system. *Curr. Biol.* **20**, R249–R254 (2010). doi:10.1016/j.cub.2010.01.026 Medline

47. S. Basu, Y. Gerchman, C. H. Collins, F. H. Arnold, R. Weiss, A synthetic multicellular system for programmed pattern formation. *Nature* **434**, 1130–1134 (2005). doi:10.1038/nature03461 Medline

48. D. Greber, M. Fussenegger, An engineered mammalian band-pass network. *Nucleic Acids Res.* **38**, e174 (2010). doi:10.1093/nar/gkq671 Medline

49. W. Ma, A. Trusina, H. El-Samad, W. A. Lim, C. Tang, Defining network topologies that can achieve biochemical adaptation. *Cell* **138**, 760–773 (2009). doi:10.1016/j.cell.2009.06.013 Medline

50. S. Basu, R. Mehreja, S. Thiberge, M.-T. Chen, R. Weiss, Spatiotemporal control of gene expression with pulse-generating networks. *Proc. Natl. Acad. Sci. U.S.A.* **101**, 6355–6360 (2004). doi:10.1073/pnas.0307571101 Medline

51. T.-L. To, B. J. Piggott, K. Makhijani, D. Yu, Y. N. Jan, X. Shu, Rationally designed fluorogenic protease reporter visualizes spatiotemporal dynamics of apoptosis in vivo. *Proc. Natl. Acad. Sci. U.S.A.* **112**, 3338–3343 (2015). doi:10.1073/pnas.1502857112 Medline

52. A. L. Szymczak, C. J. Workman, Y. Wang, K. M. Vignali, S. Dilioglou, E. F. Vanin, D. A. A. Vignali, Correction of multi-gene deficiency in vivo using a single 'self-cleaving' 2A peptide-based retroviral vector. *Nat. Biotechnol.* **22**, 589–594 (2004). doi:10.1038/nbt957 Medline

53. A. D. Cox, S. W. Fesik, A. C. Kimmelman, J. Luo, C. J. Der, Drugging the undruggable RAS: Mission possible? *Nat. Rev. Drug Discov.* **13**, 828–851 (2014). doi:10.1038/nrd4389 Medline

54. J. Downward, Targeting RAS signalling pathways in cancer therapy. *Nat. Rev. Cancer* **3**, 11–22 (2003). doi:10.1038/nrc969 Medline

55. D. C. Gray, S. Mahrus, J. A. Wells, Activation of specific apoptotic caspases with an engineered small-molecule-activated protease. *Cell* **142**, 637–646 (2010). doi:10.1016/j.cell.2010.07.014 Medline

56. J. F. Hancock, K. Cadwallader, H. Paterson, C. J. Marshall, A CAAX or a CAAL motif and a second signal are sufficient for plasma membrane targeting of ras proteins. *EMBO J.* **10**, 4033–4039 (1991). Medline

57. A. F. Oliveira, R. Yasuda, An improved Ras sensor for highly sensitive and quantitative FRET-FLIM imaging. *PLOS ONE* **8**, e52874 (2013). doi:10.1371/journal.pone.0052874 Medline

58. R. Yasuda, C. D. Harvey, H. Zhong, A. Sobczyk, L. van Aelst, K. Svoboda, Supersensitive Ras activation in dendrites and spines revealed by two-photon fluorescence lifetime imaging. *Nat. Neurosci.* **9**, 283–291 (2006). doi:10.1038/nn1635 Medline

59. A. Aronheim, D. Engelberg, N. Li, N. al-Alawi, J. Schlessinger, M. Karin, Membrane targeting of the nucleotide exchange factor Sos is sufficient for activating the Ras signaling pathway. *Cell* **78**, 949–961 (1994). doi:10.1016/0092-8674(94)90271-2 Medline

60. E. Y. C. Koh, S. C. L. Ho, Z. Mariati, Z. Song, X. Bi, M. Bardor, Y. Yang, An internal ribosome entry site (IRES) mutant library for tuning expression level of multiple genes in mammalian cells. *PLOS ONE* **8**, e82100 (2013). doi:10.1371/journal.pone.0082100 Medline

61. C. J. Wikstrand, C. J. Reist, G. E. Archer, M. R. Zalutsky, D. D. Bigner, The class III variant of the epidermal growth factor receptor (EGFRvIII): Characterization and utilization as an immunotherapeutic target. *J. Neurovirol.* **4**, 148–158 (1998). doi:10.3109/13550289809114515 Medline

62. T. S. Gardner, C. R. Cantor, J. J. Collins, Construction of a genetic toggle switch in Escherichia coli. *Nature* **403**, 339–342 (2000). doi:10.1038/35002131 Medline

63. M. B. Elowitz, S. Leibler, A synthetic oscillatory network of transcriptional regulators. *Nature* **403**, 335–338 (2000). doi:10.1038/35002125 Medline

64. J. Stricker, S. Cookson, M. R. Bennett, W. H. Mather, L. S. Tsimring, J. Hasty, A fast, robust and tunable synthetic gene oscillator. *Nature* **456**, 516–519 (2008). doi:10.1038/nature07389 Medline

65. S. J. Russell, K.-W. Peng, J. C. Bell, Oncolytic virotherapy. *Nat. Biotechnol.* **30**, 658–670 (2012). doi:10.1038/nbt.2287 Medline

66. L. Nissim, R. H. Bar-Ziv, A tunable dual-promoter integrator for targeting of cancer cells. *Mol. Syst. Biol.* **6**, 444 (2010). doi:10.1038/msb.2010.99 Medline

67. Z. Xie, L. Wroblewska, L. Prochazka, R. Weiss, Y. Benenson, Multi-input RNAi-based logic circuit for identification of specific cancer cells. *Science* **333**, 1307–1311 (2011). doi:10.1126/science.1205527 Medline

68. R. Kojima, D. Aubel, M. Fussenegger, Toward a world of theranostic medication: Programming biological sentinel systems for therapeutic intervention. *Adv. Drug Deliv. Rev.* **105** (Pt A), 66–76 (2016). doi:10.1016/j.addr.2016.05.006 Medline

69. F. Lienert, J. J. Lohmueller, A. Garg, P. A. Silver, Synthetic biology in mammalian cells: Next generation research tools and therapeutics. *Nat. Rev. Mol. Cell Biol.* **15**, 95–107 (2014). doi:10.1038/nrm3738 Medline

70. L. Bintu, J. Yong, Y. E. Antebi, K. McCue, Y. Kazuki, N. Uno, M. Oshimura, M. B. Elowitz, Dynamics of epigenetic regulation at the single-cell level. *Science* **351**, 720–724 (2016). doi:10.1126/science.aab2956 Medline

71. M. W. Kim, W. Wang, M. I. Sanchez, R. Coukos, M. von Zastrow, A. Y. Ting, Time-gated detection of protein-protein interactions with transcriptional readout. *eLife* **6**, e30233 (2017). doi:10.7554/eLife.30233 Medline

72. B. Schwanhäusser, D. Busse, N. Li, G. Dittmar, J. Schuchhardt, J. Wolf, W. Chen, M. Selbach, Global quantification of mammalian gene expression control. *Nature* **473**, 337–342 (2011). doi:10.1038/nature10098 Medline

73. C. Herrmann, G. A. Martin, A. Wittinghofer, Quantitative analysis of the complex between p21ras and the Ras-binding domain of the human Raf-1 protein kinase. *J. Biol. Chem.* **270**, 2901–2905 (1995). doi:10.1074/jbc.270.7.2901 Medline